

TOWARDS A NETWORK OF FAINT DA WHITE DWARFS AS HIGH-PRECISION SPECTROPHOTOMETRIC STANDARDS

G. NARAYAN¹, T. AXELROD³, J. B. HOLBERG², T. MATHESON¹, A. SAHA¹, E. OLSZEWSKI³, J. CLAVER¹, C. W. STUBBS^{5, 6},
R. C. BOHLIN⁴, S. DEUSTUA⁴, A. REST⁴,

Draft version March 4, 2024

ABSTRACT

We present initial results from a program aimed at establishing a network of hot DA white dwarfs to serve as spectrophotometric standards for present and future wide-field surveys. These stars span the equatorial zone and are faint enough to be conveniently observed throughout the year with large-aperture telescopes. Spectra of these white dwarfs are analyzed to generate a non-local-thermodynamic-equilibrium (NLTE) model atmosphere normalized to *HST* colors, including adjustments for wavelength-dependent interstellar extinction. Once established, this standard star network will serve ground-based observatories in both hemispheres as well as space-based instrumentation from the UV to the near IR. We demonstrate the effectiveness of this concept and show how two different approaches to the problem using somewhat different assumptions produce equivalent results. We discuss lessons learned and the resulting corrective actions applied to our program.

Subject headings: Cosmology; Observations; Methods: Data Analysis, Stars, White Dwarfs, Surveys

1. INTRODUCTION

Sub-percent global standardization of photometric calibration in astronomy remains elusive. Major ongoing and planned astronomical surveys (including LSST,⁷ PanSTARRS,⁸ SDSS,⁹ the Dark Energy Survey with DECam,¹⁰ *JWST*,¹¹ *GALEX*,¹² and *WISE*¹³) will have to attain band-to-band photometry and all-sky uniformity to better than 1% to realize their full scientific promise. As a concrete example, consider the use of Type Ia supernovae to probe the history of cosmic expansion and determine the properties of dark energy. At present, photometric calibration issues dominate the uncertainty budget on the equation of state of the dark energy, w (e.g., Sullivan et al. 2011; Suzuki et al. 2012; Betoule et al. 2014). Weak lensing tomography with LSST also demands sub-percent accuracies in color for reliable photometric redshift determination (e.g., Gorecki et al. 2014 require a systematic uncertainty of 0.005 mag or less for their photometric redshift simulations).

Most of these surveys (as well as all post-*Hubble Space Telescope* (*HST*) visible-band astronomy in the foreseeable future) are or will be pursued from the ground.

For calibration at ground-based facilities, one source of uncertainty is the time-variable transmissivity of the atmosphere, with both chromatic (Rayleigh scattering, Ozone absorption, Mie scattering, molecular absorption, aerosol) as well as gray (cloud) terms. Attenuation from clouds, water-vapor and aerosols can change rapidly and on differing angular scales and amplitudes, and over all timescales (e.g., Querel & Kerber 2014). A variety of methods are currently used to track and account for such effects including monitoring with Light Detection and Ranging (LIDAR) techniques, using dual-band Global Positioning System (GPS) metrology (e.g., Li et al. 2014), and modeling the atmosphere (e.g., with MODTRAN).

There remain, however, key obstacles to obtaining fluxes/colors in physical units at the 1% level or better:

1. Vega was one of six A0V stars used to establish the color zero point on the photometric system of Johnson & Morgan (1953) by defining the mean $U - B$ and $B - V$ color of the six stars to be zero. This definition was further extended to Cousins $R_C - I_C$. Vega's spectral energy distribution (SED) was tied to tungsten-ribbon filament lamps and laboratory blackbody sources employed as fundamental standards (Oke & Schild 1970; Hayes & Latham 1975, and references therein). The laboratory sources (placed at distances of order a mile) and Vega were observed through a telescope and spectral scanner, but corrections are necessary to account for the extinction through the atmosphere along very different paths. In particular, the wavelength-dependence of the aerosol scattering could not be ascertained with sufficient confidence and the consequent uncertainty permeates the empirical determination of Vega's SED. Alternatively, stellar atmosphere models of Vega have also been used as its intrinsic SED, in lieu of the empirical comparison against a laboratory source (especially for extension into the UV and IR). Even if the models

gnarayan@noao.edu

¹ National Optical Astronomy Observatory, 950 North Cherry Avenue, Tucson, AZ, 85719

² University of Arizona, Lunar and Planetary Laboratory, 1629 East University Boulevard, Tucson, 85721

³ University of Arizona, Steward Observatory, 933 North Cherry Avenue, Tucson, 85721

⁴ Space Telescope Science Institute, 3700 San Martin Drive, Baltimore, MD 21218

⁵ Department of Physics, Harvard University, 17 Oxford Street, Cambridge, MA, 02138

⁶ Harvard-Smithsonian Center for Astrophysics, 60 Garden Street, Cambridge, MA, 02138

⁷ <http://www.lsst.org>

⁸ <http://pan-starrs.ifa.hawaii.edu/public/>

⁹ <http://www.sdss.org>

¹⁰ <http://www.darkenergysurvey.org/>

¹¹ <http://www.jwst.nasa.gov/>

¹² <http://www.galex.caltech.edu/>

¹³ <http://wise.ssl.berkeley.edu/>

were perfect, there are other complications. Vega’s SED is punctuated with several unusually shaped absorption lines. Vega has an excess of NIR emission longwards of $1\text{--}2\ \mu\text{m}$, likely a result of its dust ring (Bohlin 2014) and possibly its rapid rotation (Peterson et al. 2006). It also has an excess of UV emission relative to a 9400K model (a result of its rapid rotation (Bohlin et al. 2014)). These may introduce systematic errors when such models are used. As a result, the absolute calibration of Vega has known deficiencies at the $\sim 1\%$ level in the visible region and at the few percent level at near IR and near UV regions (Blackwell et al. 1983; Selby et al. 1983; Mountain et al. 1985).

2. Calibrations transferred from any one primary standard to other objects around the sky using ground-based observations suffer from seasonal and site-specific systematic errors especially in the gray component of extinction through the terrestrial atmosphere. Without a well-spaced network of calibrators, “self-calibration” (Schlafly et al. 2012) or “ubercal” (Padmanabhan et al. 2008) methods cannot guarantee systemic all sky uniformity. They are especially vulnerable to any seasonal variations in declination dependence of atmospheric extinction.
3. Other currently used primary SED standards, such as BD+17°4708 and P330E, are too bright to be directly imaged by the large aperture telescopes employed by dark energy studies. Secondary standards are typically no fainter than magnitude 15, which is not within the operating dynamic range of surveys such as PanSTARRS, DES, and LSST. Indirect links require bridging across ~ 8 mags of dynamic range to calibrate the surveys. This allows various systematic errors to creep in.

The best way to circumvent the issues with the terrestrial atmospheric extinction would be to fly a standard laboratory source, such as National Institute of Standards and Technology (NIST) calibrated standard, above the atmosphere. The planning and execution of such an expensive experiment takes a long time, however, and much progress can be made towards establishing sub-percent accuracy spectrophotometry now using existing facilities and at much lower cost.

DA white dwarfs (WDs) have atmospheres dominated by hydrogen and thus are the simplest stellar atmospheres to model. The opacities are known from first principles and, in the temperature ranges (20,000–80,000K) in which we are interested, photospheres are purely radiative and photometrically stable. The SED from such an atmosphere can be defined by just two parameters: effective temperature (T_{eff}) and surface gravity ($\log g$). These parameters can be determined spectroscopically from a detailed analysis of the H I Balmer profiles, without reference to any photometry. Thus the SED, from the UV to the IR, can be calculated at arbitrary spectral resolution and used to calibrate any photometric passband or spectroscopic system. A flux normalization in any chosen passband and accurate derivation of reddening/extinction are the only other quantities required to fully characterize the received flux and establish

such objects as spectrophotometric standards. Bohlin (2014) used the *HST* Space Telescope Imaging Spectrograph (STIS) to observe three bright DA WDs spanning a range of temperatures. These objects are unaffected by reddening as interstellar absorption at Ly α implies a low H I column density, corresponding to a reddening of $E(B - V) < 0.0005$. Bohlin (2014) found their relative flux distributions to be internally consistent with model predictions from spectroscopic T_{eff} and $\log g$ to better than 1% in the wavelength range $0.2\text{--}1.0\ \mu\text{m}$. This level of internal consistency is superior to direct comparison with Vega fluxes from *HST*/STIS (Bohlin & Gilliland 2004).

The *HST* photometric scale is thus defined relative to model SEDs for 3 nearby DA WDs (Bohlin 2007). We employ the *HST* “Vegamag” photometric scale throughout this work. Holberg & Bergeron (2006) used synthetic photometry of DA WDs to place *UBVRI*, 2MASS *JHK*, SDSS *ugriz* and Stromgren *ubvy* magnitudes on the *HST* photometric scale to 1%. Holberg et al. (2008) confirmed this calibration by using a set of DA WDs with good trigonometric parallaxes that agreed at the 1% level with their photometric parallaxes from the Bergeron photometric grid.¹⁴

Modern large-telescope imaging surveys have an overlapping brightness range where the signal-to-noise ratio (S/N) is excellent for $V \sim 17\text{--}19$ mag and where these objects are unsaturated in the survey data. Thus we must extend the WD scale to fainter reference objects.

The three WDs used to define the CALSPEC calibration are bright and near enough that line of sight extinction to them can be ignored. However, the WDs in our desired brightness range are expected to have mild but easily characterizable reddening that any experiment we design must be able to quantify. There may be some faint DA WDs at 17 to 18 mag in the Galactic polar caps, but for all sky coverage, we cannot get around having to deal with extinction. Notionally, spectroscopy to derive T_{eff} and $\log g$ of suitably chosen DA WDs between 17 and 19 mag would be enough to define their SEDs. However these brightness levels place the WDs at sufficiently large distances where interstellar extinction cannot be ignored.

Alternatively we could choose a purely empirical spectrophotometric extension of the CALSPEC calibration by observing a more diverse class of objects at the desired brightness with *HST*/STIS (so that the measurements do not suffer from the effects of the terrestrial atmosphere). Such a sample could include redder objects and the question of reddening would be inconsequential as we would measure the net energy distribution. However, to build a network of a couple of dozen such stars, so that some subset of them are available at all times from all sites though a variety airmasses, would require an amount of observing time with STIS that would be prohibitively large. It would also preclude the possibility of extrapolating the calibration to wavelengths outside the range of the observations. The STIS exposure time calculator (ETC) reports integration times of several thousand seconds to reach a S/N of 100 for a 40,000K black body with $V = 18$ mag in just one of three configurations that would be minimally required to cover the wavelength range from

14

<http://www.astro.umontreal.ca/~bergeron/CoolingModels/>

3000 – 18000Å.

The approach taken by us utilizes the principle behind the CALSPEC basis for calibration, but builds up the system independently. By doing so, we also test the proposition that the DA WD models are adequate, since we intercompare results from many more objects for internal self-consistency. Our results need to stand independently of any prior calibrations to be sufficiently robust, which we think is worth the additional complications that our approach invokes.

In Table 1 we list 9 putative standard stars that are part of our Cycle 20 *HST* Program (GO 12967, P.I.: Saha), including the best available ground-based *V*-band magnitudes. Our aim in this program is to derive effective temperature, surface gravity, and interstellar reddening for these stars, that then fully parameterize (via the stellar atmosphere model) the SED incident upon the top of the Earth’s atmosphere, which is normalized with respect to the *HST* flux scale.

The essential goal of this program is to establish a set of spectrophotometrically self-consistent calibrated standard stars, tied as well as possible to an absolute physical scale. Along the way, we are empirically testing the proposition that DA WD atmospheric models result in realistic SEDs by examining whether observed flux ratios from stars with different atmospheric parameters are consistent with model predictions, after derivation and application of corrections to account for interstellar reddening. In this paper we present initial findings that define the level of consistency it is possible to achieve using these procedures.

We aim to place a select set of DA WDs between magnitude 17 and 19 on a common physical scale for flux incident at the top of the terrestrial atmosphere. This will remove uncertainties in currently used SED standards that are plagued with uncertain corrections for extinction within the terrestrial atmosphere. The expectation is that sub-percent internal consistencies can be achieved, which will be an improvement by several factors over any currently employed photometric or spectrophotometric system. A set of thus better-calibrated standard SED sources referred to a physical (absolute) system, a subset of which is always visible from any ground-based observatory, will serve as universal standard calibration sources for spectrophotometry and photometry.

In § 2 we describe the data attributes and reductions for both the *HST* imaging, as well as the ground based spectroscopy. In § 3 the photometry from the *HST* imaging is described, along with the procedure to put the measured magnitudes on the *HST* photometric scale defined by the three bright DA white dwarfs. The modeling of the emergent and received flux from each of the white dwarfs is described in § 4, as is the derivation of reddening/extinction to reconcile model and observed fluxes. In § 5 we present an alternate approach to the reconciliation of model fluxes and observed counts that bypasses some of the assumptions made in § 4 and show that the two complementary approaches produce the same results to within the accuracy limitations of the data at hand. This cross-validates some key assumptions and results of both procedures. In § 6 we present predicted magnitudes of four stars in the respective passbands of three current imaging surveys. We conclude (in § 7) with a discussion of caveats and lessons learned that have informed the

observing strategy for our *HST* Cycle 22 program.

2. OBSERVATIONS AND DATA REDUCTION

This program has three operational components. The first consists of multi-band photometry from *HST*/WFC3 images of each star that accurately tie the fluxes to the *HST* photometric scale. The second is a grid of appropriate model atmospheres to generate detailed, absolutely calibrated flux distributions and model spectra (in particular the line profiles of Balmer lines) for each star. The third is high *S/N* Balmer line spectra, nominally obtained with the Gemini Multi-Object Spectrograph (GMOS) instrument on Gemini South. The observed Balmer line profiles are analyzed in reference to the model profiles to accurately determine T_{eff} and $\log g$ for each star. The model SEDs for stars with atmospheric parameters so determined are then compared to the observed *HST*/WFC3 photometry in multiple bands, modulo a to-be-determined contribution from interstellar reddening along the line of sight to each star. The best match between model and measurement determines the reddening/extinction parameter(s).

2.1. WFC3 Observations

Wide Field Camera 3 (WFC3) observations have been obtained for all of the 9 target stars listed in Table 1. These observations yield absolute photometric fluxes in the five bands (*F*336W, *F*475W, *F*625W, *F*775W, and *F*160W) that are used to normalize the reddening corrected model spectrum that defines the stellar flux distributions. In Figure 1 we show the five WFC3 images for one of our targets, SDSS-J102430.93, along with an SDSS finder chart image of this star.

SDSS-J102430.93-003207.0

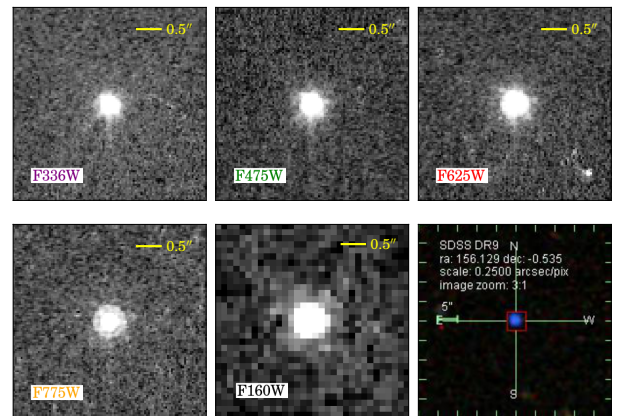


FIG. 1.— WFC3 images of SDSS-J102430.93 and an SDSS finder. Exposure times have been chosen to ensure high *S/N* in each of our five filters. Observations consist of 2–3 sub-exposures. Any observation with only 2 sub-exposures will be supplemented with an additional Cycle 22 observation. Additionally, we will obtain *F*275W observations of each target in Cycle 22.

All targets were placed near the center of the WFC3 UVIS2 detector. Each object is observed two or three times in each band with small dithers to facilitate cosmic ray rejection. The bands were chosen to ensure that the temperature, surface gravity, and reddening could be independently determined, without significant covariance.

TABLE 1
PRIMARY DA WHITE DWARF TARGETS

Object	Alternate ID	RA (J2000) h m s	Dec ° ' "	V (mag)	Spectral Observations ^a
SDSS-J010322.19-002047.7		01:03:22.1910	−00:20:47.73	19.07	G
SDSS-J041053.63-063027.7	WD-0408-066	04:10:53.6340	−06:30:27.75	18.88	GM
WD-0554-165		05:57:01.3000	−16:35:12.00	18.20	GMI
SDSS-J102430.93-003207.0		10:24:30.9320	−00:32:07.03	18.84	G
SDSS-J120650.40+020142.4	WD-1204+023	12:06:50.4080	+02:01:42.46	18.64	G
SDSS-J131445.05-031415.6	WD-1312-029	13:14:45.0500	−03:14:15.64	19.03	GM
SDSS-J163800.36+004717.7	WD-1635+008	16:38:00.3600	+00:47:17.80	18.82	G
SDSS-J203722.16-051303.0	WD-2034-053	20:37:22.1670	−05:13:03.03	18.91	G
SDSS-J232941.32+001107.8	WD-2327-000	23:29:41.3250	+00:11:07.80	18.58	G

^a References for Spectral Observations:

G = Gemini-S + GMOS

M = MMT + Blue Channel

I = Magellan Baade + IMACS

Stromgren u ($F336W$) is chosen because it sits entirely shortward of the Balmer jump and so allows a way to measure it. For our targets, the Balmer jump is sensitive to temperature. This dependency, however, is different from that of the Paschen continuum slope. The $F336W$ observations therefore help to mitigate degeneracies between reddening and temperature—a critical prerequisite for our study. $F475W$, $F625W$, and $F775W$ emulate the Sloan gri bands, respectively, and were chosen so that, in addition to measuring the Paschen continuum, they also provide a direct measure in bands being used in large surveys today (e.g., SDSS, PanSTARRS, and DES) and those planned in the future (LSST). $F160W$ is the HST /WFC3 equivalent for the H band, and it anchors measurements of our objects as far into the infra-red as HST will allow.

The exposure times were chosen to allow for S/N better than 200 for each of the targeted white dwarfs while staying shorter than half of the time to saturation. The arrangements of the various exposures times within an orbit were crafted to minimize “dead time” between exposures and optimize program efficiency. A post-flash flux was added to ensure the background level reached 12 electrons to mitigate charge transfer efficiency (CTE) losses. Additional parallel observations that include stars within a few arc-minutes from each of our target white dwarfs were obtained with the Advanced Camera for Surveys (ACS). Photometry for them, and an evaluation of their usefulness as supplementary standard stars will be presented in a future paper.

2.2. GMOS Observations

We used GMOS (Hook et al. 2004) at Gemini South to obtain moderate resolution ($R \sim 1000$), high- S/N spectroscopy of our WDs. The analysis of the detailed shape of the H I Balmer profiles ($H\beta$ to $H\zeta$) provides primary spectroscopic estimates of T_{eff} and $\log g$ that are independent of photometry or SED slopes.

The observations were obtained in queue-scheduled mode on GMOS with the B600 grating and a long slit having a width of $1''.5$. Night sky lines had a full-width at half maximum of $\sim 12\text{\AA}$. In general, there were 6×1500 s exposures made of each target. The inter-chip gaps between the three GMOS CCDs were filled by taking three observations at one grating tilt and three at another. The

entire combined spectrum contiguously covers the wavelength region between 3500 Å to 6360 Å with dispersion of 0.92 Å/pix. We resampled the spectra onto a single linear scale at 1 Å per bin. We used standard IRAF¹⁵ routines to process the CCD data and optimally extract (Horne 1986) the spectra. The overall S/N per resolution element is very high, averaging from 80 to 170 for our targets. We used our own IDL routines (Matheson et al. 2008) to flux calibrate the spectra using Feige 110 (Stone 1977). Strictly speaking, the flux calibration is not needed (and in any case rests on a less accurate basis than the ones we seek to establish), and the analysis presented in §4.1 is independent of the flux calibration of the spectra. Nevertheless, getting the continuum slopes as correct as possible helps when analyzing the shapes of the wide Balmer lines.

At this time, there are five targets (of the nine in Table 1) for which we have complete spectra and photometry. Their spectra are shown in Figure 2. One of these, SDSS-J203722.16, exhibits narrow emission lines in the cores of the Balmer absorption features. The emission lines shift with time. This could indicate the presence of a low-luminosity companion, such as an M star, although there are other possibilities. We exclude this object from all further analysis. The remaining four spectra are very characteristic of DA white dwarfs and appear free of contamination by companions.

Because the calibration standard star was not always observed contemporaneously with the targets, we validated the calibration by comparisons with the expected fluxes obtained by preliminary reddened model fluxes. In Figure 3 we show such a comparison. As discussed in §4, the method used to analyze individual Balmer profiles is relatively insensitive to any residual calibration uncertainties.

The overall response of the grating and detector yielded a count rate spectrum that peaks very near $H\beta$ and falls off significantly to the blue. At $H\zeta$ the signal is approximately 30% of peak, leading to significant S/N gradient across the Balmer lines. Fortunately the overall S/N is very high, averaging from 80 to 170 per

¹⁵ IRAF is distributed by the National Optical Astronomy Observatory, which is operated by AURA under cooperative agreement with the NSF.

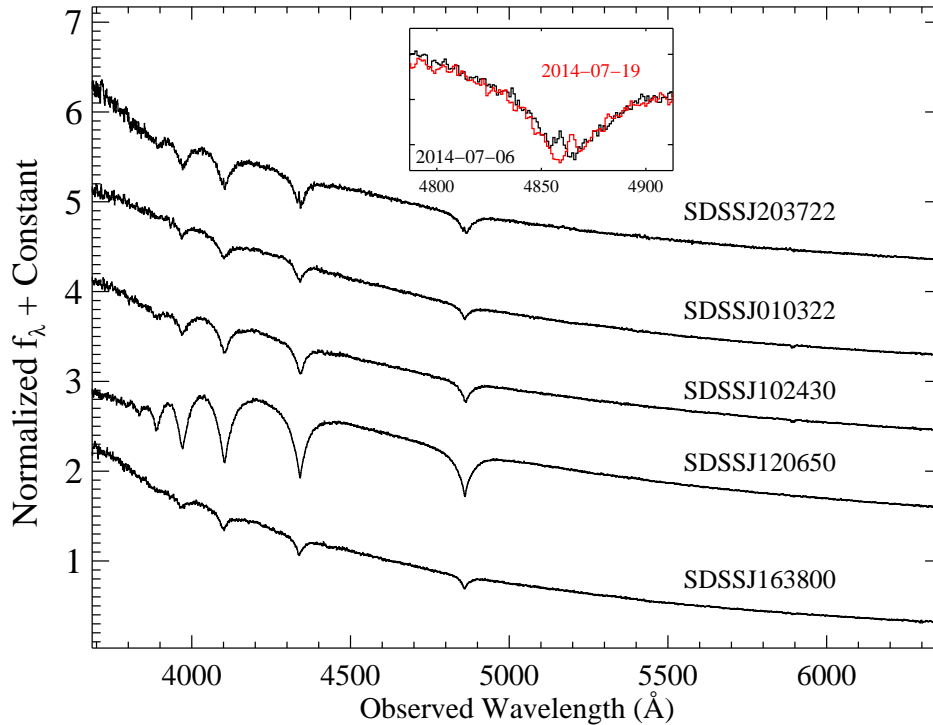


FIG. 2.— GMOS spectra of 5 of the 9 targets for which we have complete spectroscopic and photometric data. SDSS-J203722.16 has emission lines in the cores of the Balmer lines; a magnified view of the $H\beta$ line is shown in the inset for 2 epochs 13 days apart during which time the emission feature has moved by 5.3 pixels. As the observations were obtained under good seeing with a wide slit, the wavelength shift need not be solely due to a change in the relative velocity of the emission feature. Our spectra have S/N between 80–170 with a dispersion of 0.92 Å/pix . Even the weak $H\gamma$ feature is clearly resolved.

bin for our targets. For some targets, we have obtained supplemental spectroscopic observations using IMACS (Dressler et al. 2011) at Magellan, and the Blue Channel (Schmidt et al. 1989) at the MMT. They have similar S/N and resolution, and cover the same spectral range as the GMOS configuration.

3. PHOTOMETRIC ANALYSIS

As this program requires extremely accurate and precise determinations of the white dwarf flux, we have elected to use two independent methods to photometer our WFC3 observations. The drizzled (**drz**) images from the Mikulski Archive for Space Telescopes (MAST) are processed using **SExtractor** (Bertin & Arnouts 1996). The images are first masked to remove pixels in the **flt** image file that are only derived from a single exposure (determined from the **ctx** extension) and sources above the saturation threshold. A 64-pixel background mesh is used with an 8-pixel filter size to smooth the image and estimate the background locally. This procedure removes virtually all spurious objects (cosmic rays, drizzling artifacts, etc.). We use a range of apertures from 4–25 pixels to measure the flux of each source. As WFC3 has a physical image scale of $0''.04/\text{pix}$ on UVIS and $0''.13/\text{pix}$ on the IR channel, this corresponds to $0''.16$ – $1''.0$ on UVIS and $0''.52$ – $3''.25$ on the IR channel. We construct curves

of growth for each image from objects with stellar point spread functions (PSFs). We use a simple filtering routine to remove any objects that are more than 3σ away from the mean curve of growth in more than 3 apertures. This removes any objects with close companions and any non-stellar sources. We use the mean curve of growth of the image to interpolate between the measured aperture flux in each pixel to determine the precise flux with a physical aperture size of radius $0''.4$. The weight **wht** map output from **multidrizzle** is used to estimate the uncertainties.

Measurements were also made using an interactive program written by one of us (AS). A curve of growth (COG) as function of aperture size is constructed and the background level is set to be that value for which the COG is flat in the radius range 9 to 12 pixels ($0''.36$ – $0''.48$) in the UVIS images and between 6 and 8 pixels radius ($0''.78$ – $1''.04$) in the IR channel data. The ‘background’ thus measured is actually within the low level wings of the stellar PSF, but allows the use of a tight aperture so that S/N is not compromised and chances of encountering any unremoved cosmic rays or other pathologies is minimized. Using published encircled energy curves,¹⁶ measurements made this way can be corrected system-

¹⁶ http://www.stsci.edu/hst/wfc3/phot_zp_lbn

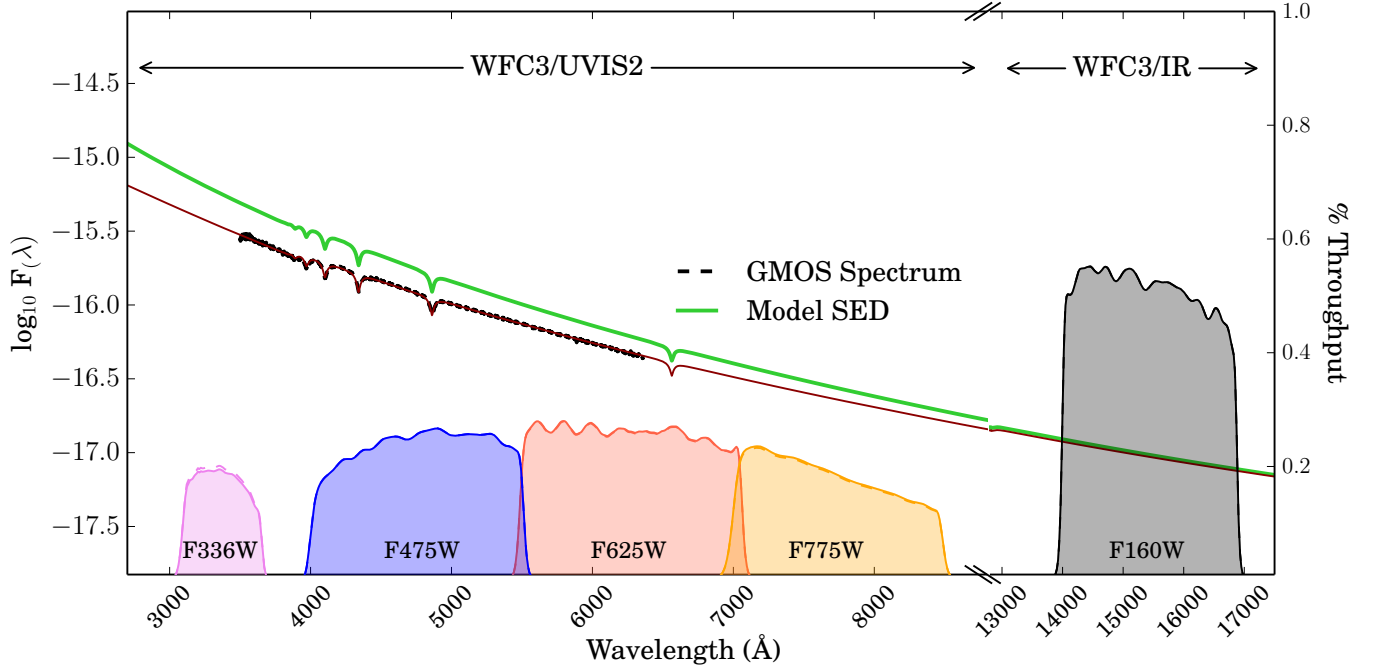


FIG. 3.— GMOS spectrum (black) along with extinguished (red) and unreddened (green) models of SDSS-J102430.93. The transmissions of the various WFC3 passbands used in our program are shown in the shaded regions. The continuum flux is removed from the spectral features before the Balmer profiles are fit. The fit model with extinction does provide an excellent match to the observed spectrum indicating that our spectroscopic flux calibration is reliable.

atically for “infinite” radius apertures (and referred to the true background), which include all of the incident light from a given object. Look-up tables for these corrections were made for each passband and applied as appropriate. These interactively made measurements, although time-consuming, are judged to be a good investment towards quality assessment because they quickly reveal the common kinds of image pathologies that defy assumptions inherent in our data models. These interactive measurements were made on both `flt` and `drz` images, where the `flt` images were corrected for variations in pixel area. Concordant measurements on both sets of images indicate whether the `multidriz` process compromises data quality (e.g., by being overzealous about CR rejection and cropping the tips of bright stars). Agreement across the two measuring methods establishes that methodology-dependent systematic errors are not being injected.

As the WFC3 detector sensitivity is a function of time, the zeropoints are time dependent. Rather than rely on the fiducial zeropoints supplied by MAST, we measured the zeropoints directly using contemporaneous observations of CALSPEC primary standard, GD153, obtained through *HST* GO program 13575 (P.I.: S. Deustua). These are applied as an additive adjustment to the fiducial MAST zeropoint. Subrastered images of GD153 are available with the target at the same position on the detector as our DA white dwarfs, however not in all of our passbands (*F775W* is missing). We are obtaining contemporaneous observations of all three primary standards in Cycle 22 to determine instrumental zeropoints, and tie our measurements directly to this photometric system.

In this work, we have measured GD153’s instrumen-

tal magnitudes using the same process for our targets, as described above. We applied the fiducial MAST zeropoints to our instrumental magnitude, and compared these magnitudes against synthetic photometry of the CALSPEC model of GD153 (`gd153_fos_003`)¹⁷ through the WFC3 passbands. The synthetic photometry is described in §4, by Equation 5. While this procedure is not as optimal as tying our measurements directly to the three *HST* primary standards, it is best methodology possible given the extant data.

We found a difference between the synthetic and measured magnitudes that exhibits a strong linear trend with passband frequency. The measurements in each passband, and the linear trend is shown in Figure 4. There is no process through which our measurement technique, which treats all the images individually, can introduce such a linear trend with frequency. The largest discrepancy was found in the ultraviolet and the smallest differences in the optical. No significant difference was found in the WFC3/IR channel, which has a completely different detector and light path through the camera. The observed trend therefore indicated a possible difference between the reported and true efficiency of the UVIS detectors.

This finding was independently replicated by staff scientists at STScI. As the two WFC3/UVIS CCDs were manufactured on different wafers and foundry production runs, their physical properties, such as quantum efficiency and thickness, differ. Studies at STScI have found that UVIS2 is $\sim 30\%$ more sensitive in the UV than UVIS1. In the range $3500 - 7000\text{\AA}$, the two CCDs have comparable sensitivity, while at wavelengths longer

¹⁷ ftp://ftp.stsci.edu/cdbs/calspec/gd153_fos_003.fits

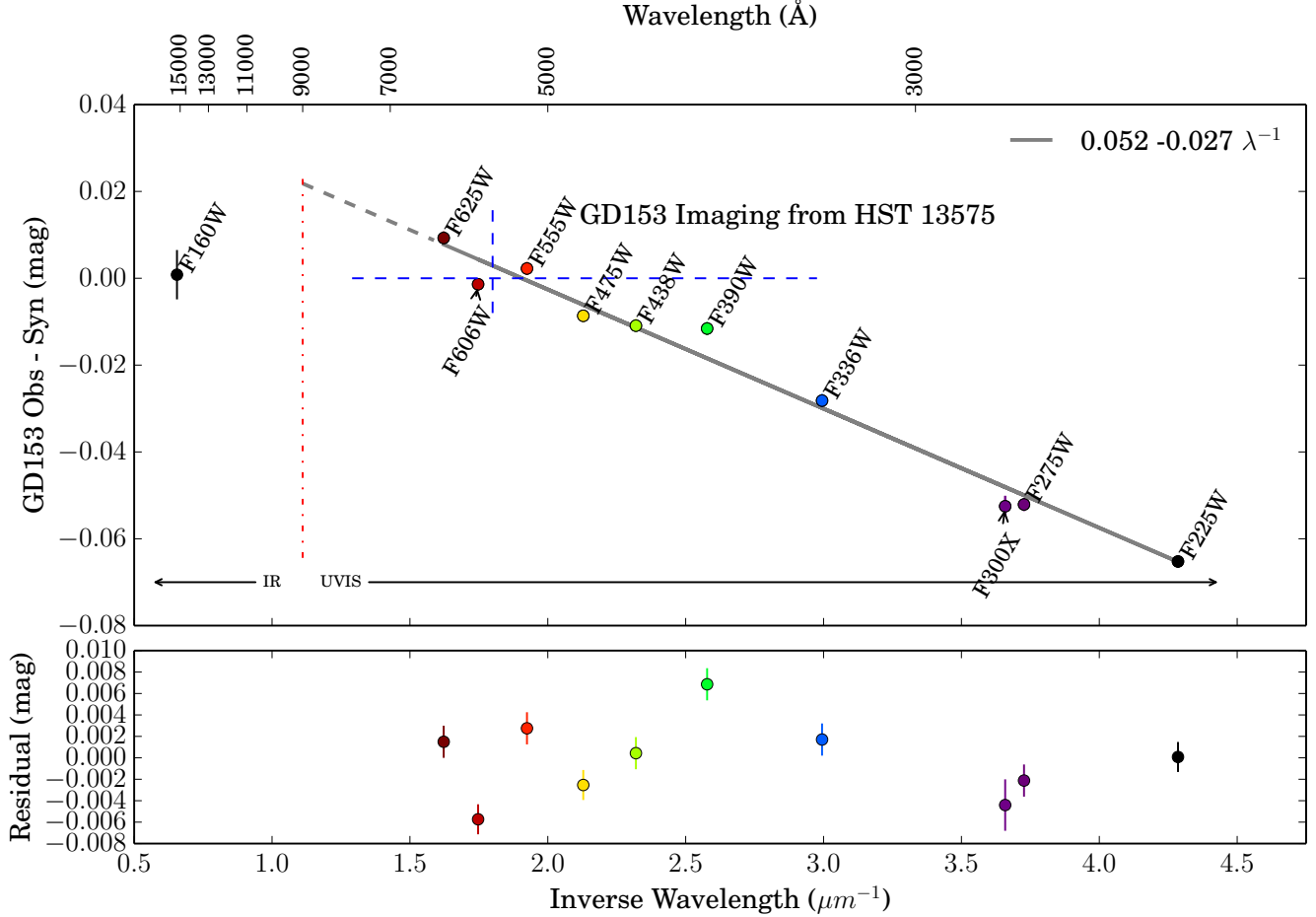


FIG. 4.— (Top) Differences between measured magnitudes with fiducial MAST zeropoints and synthetic CALSPEC magnitudes for GD153 (*HST* program GO 13575, P.I. S. Deustua). We found a strong linear trend with frequency, indicating a difference between the zeropoints reported by MAST (which are the same for UVIS1 and UVIS2), and the true zeropoint. (Bottom) Residuals to the linear fit to the data are typically below 0.005mag. The trend with frequency suggests that this effect is likely a result of differing quantum efficiencies of the two UVIS detectors. This finding was independently verified by STScI staff scientists and will be corrected with new flat-field calibrations applied to future *HST* data products.

than 7000Å, UVIS1 is a few percent more sensitive. Furthermore, the two detectors have different detection layer thicknesses. For UVIS1 the median thickness is 16.04 ± 0.23 microns, and for UVIS2 it is 15.42 ± 0.58 microns¹⁸.

New flat-fields that treat the two UVIS detectors individually have been created and will be applied to future MAST products. For this work, we correct the fiducial MAST zeropoints for each of our passbands with the linear relation we found. These corrected zeropoints are applied to the measured flux to produce the observed magnitudes for the targets used in this work. The photometry and measurement uncertainties for these targets is listed in column 3 of Table 2. The measured magnitudes are therefore described by

$$m_{T,i}^O = -2.5 \log_{10}(\phi_{T,i}^O) + ZP_T^{\text{MAST}} + \Delta ZP_T^{\text{GD153}} \quad (1)$$

where m is the natural magnitude, ϕ the measured flux of the object, i , ZP_T^{MAST} is the instrumental zero point

published in MAST, and $\Delta ZP_T^{\text{GD153}}$ is the correction to the fiducial MAST zeropoint derived, as described above, using observations and synthetically predicted photometry of GD153, observed through passband T . “O” is used to denote observed quantities.

4. MODELING

4.1. Line Profile Fitting

We have analyzed the Balmer profiles of each star in a manner similar to that described by Bergeron et al. (1992) and Liebert et al. (2005). We use *Tlusty* NLTE model atmospheres (Hubeny & Lanz 1995) (version 203)¹⁹ to match the models used by Bohlin et al. (2014). Each Balmer profile is individually extracted with a window centered on the profile and extending well into the wings. These extracted profiles are ‘flattened’ by constructing a linear interpolation between fixed points in the far wings of the profiles. This flattening places the burden of determining T_{eff} and $\log g$ solely on the

¹⁸ <http://www.stsci.edu/~INS/2010CalWorkshop/wong.pdf>

¹⁹ <http://nova.astro.umd.edu/Tlusty2002/tlusty-frames-down.html>

TABLE 2
DA WHITE DWARF OBSERVED MAGNITUDES, FIT PARAMETERS, AND SYNTHETIC MAGNITUDES

Object Name	Passband	Observed Magnitude ^a	A_V	T_{eff}	$\log g$	Synthetic Magnitude	Extinction ($R_V = 3.1$)	Extinguished Magnitude	Residual
(1)	(2)	(mag) (3)	(mag) (4)	(Kelvin) (5)	(6)	(mag) (7)	(mag) (8)	(mag) (9)	(mag) (10)
SDSS-J010322.19	<i>F336W</i>	17.344 (0.003)				17.176 (0.001)	0.171	17.347 (0.008)	−0.003
	<i>F475W</i>	19.189 (0.003)				19.058 (3E-4)	0.125	19.183 (0.006)	+0.006
	<i>F625W</i>	19.424 (0.003)	0.101	59530	7.53	19.340 (4E-5)	0.088	19.428 (0.004)	−0.004
	<i>F775W</i>	19.588 (0.004)	(0.005)	(260)	(0.02)	19.522 (7E-5)	0.068	19.590 (0.003)	−0.002
	<i>F160W</i>	20.105 (0.005)				20.081 (7E-5)	0.021	20.102 (0.001)	+0.004
SDSS-J102430.93	<i>F336W</i>	17.315 (0.004)				16.856 (7E-4)	0.453	17.309 (0.008)	+0.006
	<i>F475W</i>	19.004 (0.003)				18.679 (1E-4)	0.331	19.010 (0.006)	−0.006
	<i>F625W</i>	19.170 (0.003)	0.269	40620	7.75	18.937 (1E-4)	0.234	19.171 (0.004)	−0.002
	<i>F775W</i>	19.291 (0.003)	(0.005)	(124)	(0.01)	19.111 (2E-4)	0.180	19.291 (0.003)	−0.001
	<i>F160W</i>	19.718 (0.005)				19.658 (2E-4)	0.055	19.712 (0.001)	+0.005
SDSS-J120650.4	<i>F336W</i>	17.301 (0.003)				17.213 (0.002)	0.089	17.302 (0.013)	−0.000
	<i>F475W</i>	18.776 (0.002)				18.708 (4E-4)	0.064	18.773 (0.009)	+0.003
	<i>F625W</i>	18.912 (0.002)	0.052	23650	7.89	18.871 (1E-4)	0.046	18.916 (0.006)	−0.004
	<i>F775W</i>	19.033 (0.003)	(0.008)	(46)	(0.01)	19.000 (2E-4)	0.035	19.035 (0.004)	−0.002
	<i>F160W</i>	19.443 (0.004)				19.428 (2E-4)	0.011	19.439 (0.001)	+0.004
SDSS-J163800.36	<i>F336W</i>	17.113 (0.003)				16.778 (0.001)	0.337	17.115 (0.008)	−0.002
	<i>F475W</i>	18.925 (0.002)				18.676 (2E-4)	0.247	18.923 (0.006)	+0.002
	<i>F625W</i>	19.136 (0.003)	0.200	64610	7.43	18.961 (5E-5)	0.174	19.135 (0.004)	+0.001
	<i>F775W</i>	19.279 (0.003)	(0.005)	(425)	(0.02)	19.144 (9E-5)	0.134	19.278 (0.002)	+0.001
	<i>F160W</i>	19.743 (0.004)				19.704 (9E-5)	0.041	19.745 (0.001)	−0.002

^a All magnitudes are reported in the HST VEGAmag system. Uncertainties are quoted in parentheses

quasi-symmetrical line profiles and decouples the analysis from temperature dependent slopes in the underlying SED. The model profiles are flattened in precisely the same fashion. Minimum χ^2 fits are sought between models and observations and contours enclosing 68% and 95% of the total likelihood around the maximum likelihood estimate are constructed. The profiles, fit, and likelihood surface for SDSS-J102430.93 are shown in Figure 5.

The likelihood surfaces show very low covariance between T_{eff} and $\log g$. This is unsurprising as the two parameters change the shape of the Balmer profiles in distinct ways. Uncertainties are directly estimated from the 1-D marginalized likelihoods for both parameters. As the spectra have to be dereddened before the line profiles are fit, we also examine the covariance between T_{eff} and $\log g$ and the fiducial value of $E(B - V)$ used to deredden the spectrum, derived from SDSS DR12 photometry. We find a weak linear covariance of both T_{eff} and $\log g$ over a range of ± 0.05 in $E(B - V)$. This range in $E(B - V)$ is much larger than the uncertainty in the value determined from our WFC3 photometry. We find that the maximum difference in the best fit values for T_{eff} and $\log g$ over the entire range of $E(B - V)$ are less than 0.3 of the uncertainty in T_{eff} and $\log g$. The changes in χ^2 over the same value are not statistically significant and reflect the different centering of the grid of T_{eff} and $\log g$ over which the minimum chi-squared fit is determined. This demonstrates that the temperature and surface gravity determined from spectra are completely insensitive to the fiducial interstellar $E(B - V)$ used to deredden the spectrum.

Our methodology is insensitive to the choice of model. While model atmospheres are generated as a function of T_{eff} and $\log g$, these are nuisance parameters that serve

as labels for a specific line shape. Two different models may have different values of T_{eff} and $\log g$ for the same line shape. Our procedure is only affected by *relative* flux differences at constant line shape. We estimate the systematic error arising from the choice of a specific set of model atmospheres by fitting the Rauch et al. (2013, hereafter RWBK) models for the *HST* primary standards derived in Bohlin (2014). We fit the RWBK models using the same procedure as the observed white dwarf spectra. The resulting model atmospheres are normalized at 5556Å. The relative flux ratios are shown in Figure 6.

The *Tlusty* models at the fiducial temperature and surface gravity of the RWBK model are a close match to the Bohlin (2014) models. Fitting the line profiles of the RWBK models improves the agreement between the two models, and the synthetic photometry difference is less than 0.003 mag in all passbands. The residual difference in the line shape arises from a difference in the shapes of the line profiles between the RWBK and *Tlusty* models, likely a result of the different prescriptions used for Stark broadening. Sharp discontinuities in the relative flux ratio arise from differences in the continuum between the two models. This is most evident in the models of G191B2B. Both models are interpolated from model atmosphere grids, piece-wise over different wavelength ranges, and these different sections are combined together to create a model atmosphere spanning the full wavelength range at the desired values of T_{eff} and $\log g$. These discontinuities reflect differences in the grids and the different interpolation schemes adopted by the two models, rather than any difference in the underlying physics.

4.2. Synthetic Photometry and Interstellar Reddening

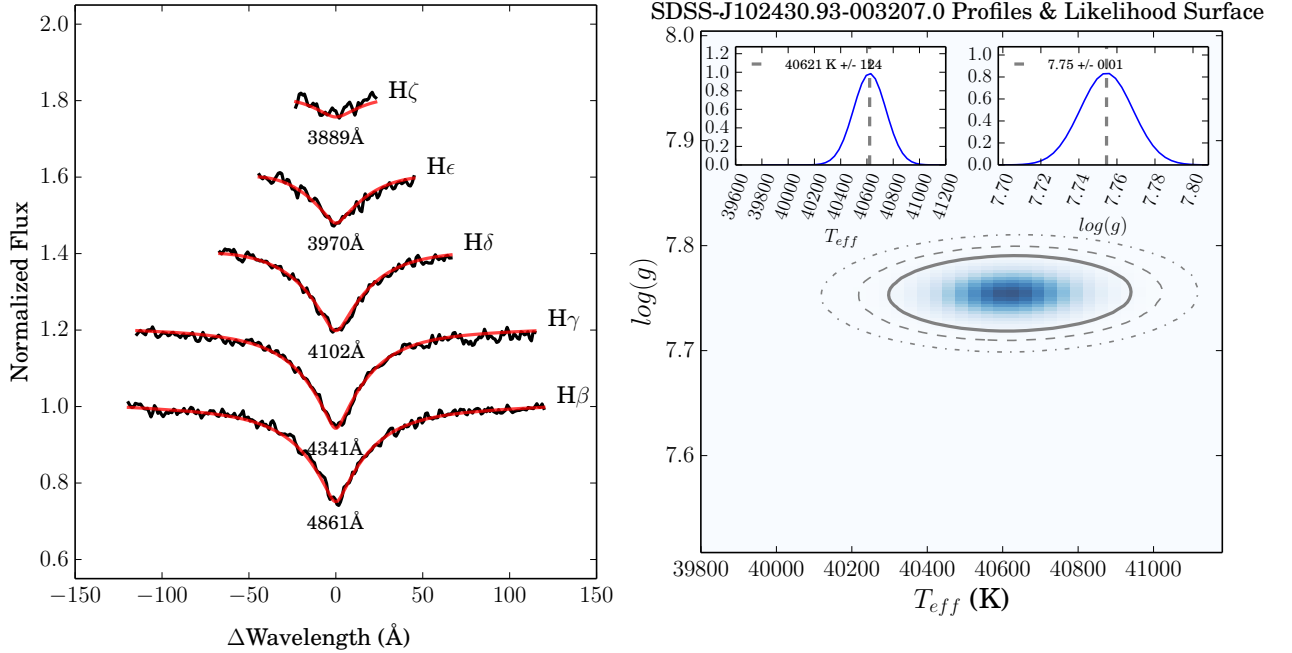


FIG. 5.— (Left) Balmer line profiles extracted from the GMOS spectrum (black) and model fits (red) for SDSS-J102430.93, the same object shown in Figure 3. The central wavelength of each feature is indicated below the line. Small vertical offsets have been added to the continuum of each line for visualization. Even the extremely weak H ζ feature is well modeled. (Right) The log likelihood surface in T_{eff} - $\log g$ space for the fit are shown along with contours enclosing 68%, 95%, and 99.7% of the likelihood surface around the maximum likelihood estimate (solid, dashed, and dot-dashed, respectively). Marginalizations are shown in the inset plots. The 1-D distributions are well-modeled by Gaussians and the peak is indicated in the legend. There is virtually no covariance between the two parameters, indicating that are observations are sufficient to constrain both independently.

In most prior work on photometric standards, interstellar reddening has not been a significant issue. The stars presented here, though, are from one to three magnitudes fainter and significantly more distant so interstellar reddening needs to be considered, estimated, and applied. Our working model is to assume that the DA white dwarf models correctly predict the emergent flux from the star, and so the difference between observed magnitudes and model predictions must show the color signature from the Galactic reddening law. Since we have photometry in multiple bands, failure of either the Galactic reddening law, or of the SED model for emergent flux, will show up as discrepancies. If all the passbands are consistent with these assumptions, then the SED model plus the reddening/extinction value fully describes the received SED from the white dwarf. Accordingly we proceed as described below.

4.2.1. Synthetic Photometry

With the best fit temperature and surface gravity, we generate a full model SED for the white dwarf, from 1300-25000Å. We use the `pysynphot` package,²⁰ and convolve the model SED with the response function of the observed *HST* passbands. We model the passband transmissions as the product of three components: the optical train (Opt), the filter (PB) and the Quantum Efficiency of the WFC3 detectors (OE).

$$T(\lambda) = T_{\text{Opt}}(\lambda) \times T_{\text{PB}}(\lambda) \times \text{QE}(\lambda) \quad (2)$$

The published passband transmissions are based on pre-flight laboratory measurements, and represent the fiducial system throughput. In principle, it is possible to determine the count-rate yielded by an object with an $F(\lambda)$ spectrum throughput by simply computing the integral of the flux through the passband. However, all three components of the transmission are time variable, and this is reflected in periodic updates to the published MAST zeropoints. We therefore derive synthetic zeropoints for each passband, T , using the definition of the *HST* “Vegamag” system that defines Vega to have a magnitude of zero at all wavelengths. The synthetic flux, and magnitude, ϕ , and m , respectively, is given by

$$\phi_{T,i}^S = \frac{\int_0^\infty \lambda F_i^S(\lambda) T(\lambda) d\lambda}{\int_0^\infty \lambda T(\lambda) d\lambda} \quad (3)$$

$$\phi_{T,\text{Vega}}^S = \frac{\int_0^\infty \lambda F_{\text{Vega}}^S(\lambda) T(\lambda) d\lambda}{\int_0^\infty \lambda T(\lambda) d\lambda} \quad (4)$$

$$\begin{aligned} m_{T,i}^S &= -2.5 \log_{10}(\phi_{T,i}^S) + \text{ZP}_T^{\text{Vega}} \\ &= -2.5 \log_{10}(\phi_{T,i}^S) + 2.5 \log_{10}(\phi_{T,\text{Vega}}^S) \\ &= -2.5 \log_{10} \left(\frac{\int_0^\infty \lambda F_i^S(\lambda) T(\lambda) d\lambda}{\int_0^\infty \lambda F_{\text{Vega}}^S(\lambda) T(\lambda) d\lambda} \right) \end{aligned} \quad (5)$$

where “S” is used to indicate synthetic quantities. The resulting synthetic magnitudes are tied to Vega. The SED, $F^S(\lambda)$, is not adjusted by the distance and radius of the white dwarf and thus is unreddened. The red-

²⁰ <http://stdas.stsci.edu/pysynphot/>

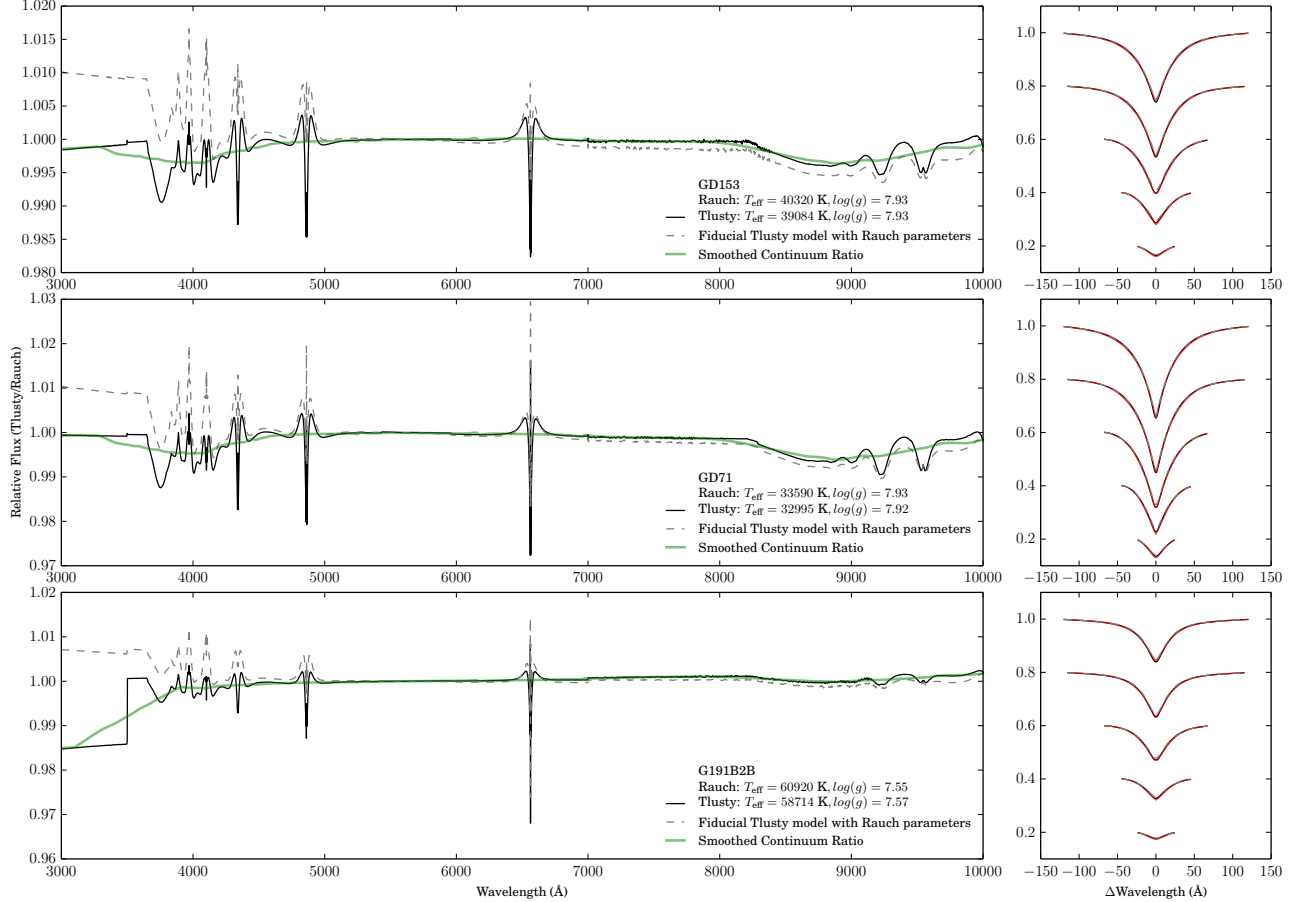


FIG. 6.— Comparison of *Tlusty* (Hubeny & Lanz 1995) and Rauch et al. (2013) (RWBK) models of *HST* primary spectrophotometric standards GD153 (top), GD71 (middle) and G191B2B (bottom). The dashed gray line indicates the relative flux ratio between the two models at the fiducial T_{eff} and $\log g$ determined by Bohlin (2014). Fitting the line profiles of the RWBK models using the *Tlusty* models improves the agreement between the two sets of models (solid black lines). The residual differences are dominated by small differences in the shapes of the line profiles between the two models, likely because of different prescriptions used to model Stark broadening. Overall, the line profile shapes are very similar (right panels). As these differences are small and nearly symmetric about unity, they do not contribute significantly to any net flux difference. We use a Savitzky-Golay filter to smooth the relative flux ratio and highlight regions where the models disagree (solid green lines). There are, however, no significant departures from unity. Discontinuities in the flux ratio in the UV arise from differences in the interpolation schemes adopted by the two models and are only significant in the $F336W$ flux for G191B2B. A change in the T_{eff} of the *Tlusty* model of under +1000K is sufficient to reduce the effect of the discontinuity to less than 0.001 in the relative flux ratio.

dening and normalization for the distance, and radius is treated in §4.2.2. We use the CALSPEC composite stellar spectrum of Vega (`alpha_lyr_stis_005`)²¹ as our model for Vega’s SED, F_{Vega}^S . The CALSPEC model for Vega, and GD153 used in §3 are normalized consistently internally, and thus synthetic magnitudes produced relative to the Vega model are directly comparable to the observed magnitudes that have been tied to GD153. In Cycle 22, we will obtain observations of all three primary standards in all of our bands, and tie our observations to the average of all three, obviating the need to put our observations on the “Vegamag” system.

4.2.2. Interstellar Reddening

We compute the difference between the observed and synthetic magnitudes for each star, and fit these with i) a constant to account for the normalization that is the same at all wavelengths (and reflects the radius of and

distance to the white dwarf), and ii) a slope corresponding to a scaling of the Fitzpatrick (1999) reddening law, with the canonical $R_V = 3.1$, appropriate for the Milky Way. The extinction values in each passband are given by the weighted extinction for each band as calculated via:

$$m_{T,i}^O - m_{T,i}^S = A_T(\langle\lambda\rangle) * A_V^i + c_i$$

$$\langle\lambda\rangle = \frac{\int_0^\infty \lambda^2 T(\lambda) d\lambda}{\int_0^\infty \lambda T(\lambda) d\lambda} \quad (6)$$

where $A(\langle\lambda\rangle)$ is the extinction computed at the effective wavelength of the passband T , $\langle\lambda\rangle$, defined for unit $E(B - V)$, again using the extinction of Fitzpatrick (1999) for $R_V = 3.1$, and c_i is a wavelength-independent constant to account for a passband independent overall brightness normalization for each white dwarf. The normalization constant, c_i , must be added to the synthetic magnitudes, $m_{T,i}^S$, to compute correctly normalized mag-

²¹ http://ftp.stsci.edu/cdbs/calspec/alpha_lyr_stis_005.fits

nitudes.

The results of applying the above procedure to the four DA white dwarfs for which the spectroscopic and photometric data are complete (discarding the discrepant object with the emission components in the Balmer lines) are shown in Table 2 and graphically in Figure 7. Included in the Table are the three fitted parameters, A_V , T_{eff} , and $\log g$, intrinsic normalized magnitude before reddening, the extinction in each band, and the net predicted magnitude per band. Both synthetic quantities include the normalization constant, c_i . Comparison of column 9 with column 3 (predicted vs. observed magnitudes with WFC3/*HST*) corresponds to the fit residuals per band given in column 10. Note that the extreme residuals are $+/-0.006$ with rms = 0.003 mag.

If we use the extinction law of O'Donnell (1994) instead of Fitzpatrick (1999), the derived A_V values change by 1 milli-mag, thereby indicating that our experiment is insensitive to differences between these forms of the reddening law.

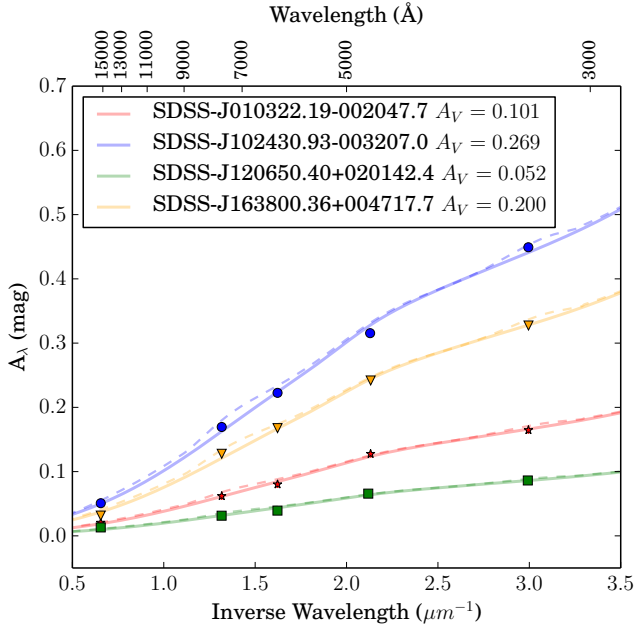


FIG. 7.— Extinction curve fits with $R_V = 3.1$ using the reddening law of Fitzpatrick (1999) (solid) and O'Donnell (1994) (dashed) for four objects in our sample, spanning a range from low to high reddening. The largest differences in the derived value of A_V using the two different extinction laws is seen for SDSS-J010322.19-002047.7 and SDSS-J120650.40+020142.4 where it is 0.001 mag. The mean residuals between the data and the fit extinction curve are 3 mmag.

5. ALTERNATE APPROACH TO SYNTHETIC PHOTOMETRY AND INTERSTELLAR REDDENING

The above analysis is contingent on the state of calibration of WFC3, and the assertion that CALSPEC standards have SEDs known very accurately. The shape of the WFC3 passbands is implicitly assumed to be correct. The SED of GD153, a DA white dwarf itself, is used to adjust the overall normalization of the effective passbands, and the CALSPEC SED of Vega is used to

establish the zeropoints of color. These assumptions create a formal dependency on the state of calibration of WFC3, and on the currently adopted SEDs of GD153 and Vega. The “constructionist” approach taken in the above section is thus vulnerable to the state of calibration of WFC3. Thus, we have had to correct the zeropoints, as in equation 1.

However, there is indication that the WFC3 zeropoints are uncertain at the 0.01 mag level. For example, the current MAST zeropoints are prefaced by a discussion that states “The tables below summarize results determined from a new reduction of all SMOV4, Cycle 17, and Cycle 18 observations of GD153, G191B2B, GD71, and P330E. The independent calibrations from the four stars agree to within 1% in most filters, and the photometric zeropoint is set to the average of the measurements.” All four of these stars have nominally zero reddening, and have equal weight in the determination of the WFC3 zeropoints.

Given this reality, and our goal of achieving precisions substantially better than 1%, we have explored an alternate approach to optimally determining the reddening and SEDs of our white dwarfs. In this approach, we determine an optimal set of stellar parameters and passband-dependent aperture corrections by fitting the synthetic magnitudes for all stars simultaneously to the observed instrumental magnitudes, including for each star an extinction value and a passband-independent zeropoint. The only assumptions here are that DA white dwarf models do predict SEDs accurate to a few millimag or better, the standard Galactic reddening law is valid for our targets, the published WFC3 passbands are approximately correct in shape, and the bright DA white dwarf GD153 has zero reddening.

We develop the following formalism, using the same notation adopted in § 4.2.

The instrumental magnitude is just $-2.5 \log_{10} N$, where N is the count rate of detected electrons.

$$N_{T,i} = k \int_0^\infty \lambda F_i^O(\lambda) T(\lambda) d\lambda \quad (7)$$

where k is a *band independent* constant that depends only on the telescope aperture. We can write:

$$m_{T,i}^X = -2.5 \log_{10} k - 2.5 \log_{10} \int_0^\infty \lambda F_i(\lambda) T(\lambda) d\lambda \quad (8)$$

We subsequently use $K = -2.5 \log_{10} k$.

To compare a synthetic magnitude to a measured *HST* instrumental magnitude, the synthetic magnitude is defined in terms of the model flux, $F_i^S(\lambda)$ as

$$m_{T,i}^S = -2.5 \log_{10} \int_0^\infty \lambda F_i^S(\lambda) T(\lambda) d\lambda \quad (9)$$

We define another *band independent* constant, C_i , to account for the geometry (radius of the star, and distance to the star) that modulates for each target star, the flux at the stellar surface to that incident at the top of the terrestrial atmosphere. The instrumental magnitude, m^X , can then be written in terms of synthetic (S) quantities as:

$$m_{T,i}^X = K - 2.5 \log_{10} C_i^{X,S} - 2.5 \log_{10} \int_0^\infty \lambda F_i^S(\lambda) T(\lambda) d\lambda \quad (10)$$

Denoting $K - 2.5 \log_{10} C_i^{X,S}$ by $K_i^{X,S}$ this is simply:

$$m_{T,i}^X = K_i^{X,S} + m_{T,i}^S \quad (11)$$

If the model fluxes are correct, the synthetic instrumental magnitudes will equal the observed instrumental magnitudes. However, the synthetic magnitudes implicitly count all photons detected from the object, regardless of where they end up in the PSF, while the observed magnitudes count detected photons only within a finite radius ($0''.4$ in our case). The resulting difference is the aperture correction and is band dependent because the PSF is. A nominal value of the aperture corrections is available from MAST, but we leave them as values to be determined from the data. Denoting the aperture correction as Δ_T , we then expect that

$$m_{T,i}^X = K_i^{X,S} + m_{T,i}^S + \Delta_T \quad (12)$$

or, expressed another way,

$$\delta_{T,i} \equiv m_{T,i}^X - m_{T,i}^S - \Delta_T = K_i^{X,S} \quad (13)$$

Note that, although we expect the dominant contribution to Δ_T to come from the aperture correction, *any* bandpass dependent error, including putative errors in calibrating the instrument, will contribute. The dependence of $\delta_{T,i}$ on the passband, T , is a powerful diagnostic. Equation 13 tells us that the wavelength dependence should be fully accounted for by the aperture correction, and the synthetic model. If there is a discrepancy, it can arise from several causes:

- The aperture corrections Δ_T are incorrect.
- There is extinction affecting the real object that is not represented in the model.
- The model fluxes have errors not accounted for by extinction.

Given the distance to our stars, it is likely that they will be affected by some amount of extinction (interstellar, and possibly circumstellar), we can fit for the reddening, and analyze the remaining residuals for the other causes listed above. The extinguished synthetic magnitude is:

$$m_{T,i}^S = -2.5 \log_{10} \int_0^\infty \lambda F_i^S(\lambda) \alpha_i(\lambda) T(\lambda) d\lambda \quad (14)$$

where $\alpha_i(\lambda)$ is the transmission function of the extinction for object i .

We parameterize $\alpha_i(\lambda)$ in terms of the quantities R_V and $E_{(B-V,i)}$, and calculate it by the prescription of O'Donnell (1994). We can then determine the extinction parameters, along with the Δ_T and $K_i^{X,S}$ by minimizing

$$\begin{aligned} \chi^2(\{E_{B-V,i}\}, \{K_i^{X,S}\}, \{\Delta_T\}) = \\ \sum_{T,i} (m_{T,i}^X - m_{T,i}^S - \\ - A_T \times R_V \times E_i(B-V) \\ - \Delta_T - K_i^{X,S})^2 \end{aligned} \quad (15)$$

with the constraint that $E_{B-V,i} \geq 0 \forall i$.

With our current four stars and 5 WFC3 passbands, χ^2 depends on 12 parameters, while we have 20 measurements, so the minimization problem is potentially well constrained. Additional stars and/or passbands will constrain the solution further. We keep $R_V = 3.1$ for the present, although it could in principle be included in the parameters being optimized.

There are two difficulties with this approach, however. The first one is trivial. There is a partial degeneracy between the Δ_T and $K_i^{X,S}$, in that an arbitrary constant can be added to all the Δ_T and then subtracted from all the $K_i^{X,S}$ without changing the value of χ^2 . This needlessly complicates the job of the optimizer, and makes the results harder to interpret. We deal with this by enforcing

$$\sum_T \Delta_T = 0 \quad (16)$$

The second difficulty is more serious. Experience with minimizing χ^2 as given above shows that the minimum is consistently achieved by choosing the Δ_T so that the extinction of the least extinguished star comes out to be zero. This is readily achieved, since the right choice for Δ_T can mimic an arbitrary extinction, that is then effectively subtracted from the extinctions of all the stars. This behavior is unphysical, and must be remedied by an additional data-based constraint. We have chosen to use the observations of GD153 discussed in Section 3 in conjunction with the conclusion of Bohlin et al. (2014) that its extinction is zero to high precision.

To make use of this constraint, we treat the GD153 data in the same way as the program stars, but its contribution to χ^2 is treated differently in that when calculating the model flux, $E_{B-V, \text{GD153}} = 0$ by assumption. The GD153 contribution to the overall χ^2 is multiplied by a weighting factor large enough to ensure that any significant deviation from this assumption is suppressed. The summation over bands includes only $F336W$, $F475W$, and $F625W$, since we currently lack GD153 data for the other bands. The model flux for GD153 uses the G11 values for T_{eff} and $\log g$ from Bohlin (2014).

$$\chi_{\text{GD153}}^2 = w_{\text{GD153}} \sum_i (m_{T,\text{GD153}}^X - m_{T,\text{GD153}}^S - \Delta_T - K_{\text{GD153}}^{X,S})^2 \quad (17)$$

The weighting factor $w_{\text{GD153}} = 1/0.01^2$ for the results quoted below ensures that the GD153 reddening is very close to zero.

5.1. Results

The χ^2 minimization of equation (15) was carried out using IDL routine `CONSTRAINED_MIN`. To perform error

TABLE 3
FIT RESULTS FOR PRIMARY DA WHITE DWARF
TARGETS

Object	A_V	σ_{A_V} (mag)	$\sigma(fit)$
SDSS-J010322.19-002047.7	0.095	0.005	0.007
SDSS-J102430.93-003207.0	0.264	0.005	0.004
SDSS-J120650.40+020142.4	0.051	0.008	0.004
SDSS-J163800.36+004717.7	0.197	0.005	0.006

analysis of the results, the minimization was carried out a large number of times using independent samples from Gaussian distributions of T_{eff} , $\log g$ and $\{m_{T,i}^O\}$. The covariance matrix for these quantities is assumed to be diagonal. The uncertainties in the distributions come from Table 2. Table 3 shows the resulting mean values of A_V for the four stars, their statistical uncertainties, and the mean standard deviation of the fit to the observed magnitudes for each star. Table 4 presents the mean values of the derived aperture corrections, Δ_T , for the five WFC3 bands we employ, and the nominal values from MAST. It is noteworthy that the agreement between our derived aperture corrections, Δ_T , and the fiducial MAST values is excellent, with discrepancies of order 0.01 mag, as expected.

Comparison with A_V values in Table 3 with those in Table 2 that are derived by the other procedure shows differences of a few millimag, with consequent differences in SED fluxes over the observed passband range of 10 or 20 millimag. We expect that with the Cycle 22 data, which includes observation in $F275W$ and contemporaneous constraining observation of all three *HST* white dwarf calibrators, the SEDs from both approaches will result in closer agreement for the derived final SEDs. We emphasize that all quoted uncertainties are purely statistical.

6. EXPECTED MAGNITUDES ON COMMON PHOTOMETRIC SYSTEMS

As our targets are within the dynamic range of present wide-field survey facilities, we provide expected synthetic magnitudes for SDSS, PanSTARRS, and DECam photometric systems in Table 5. The passband throughputs used to synthesize magnitudes include the attenuation from the terrestrial atmosphere at a representative airmass of 1.3 at the respective observatory sites. Where available, we have compared our synthetic photometry to published photometry from surveys from their respective facilities.

In all cases we quote magnitudes on the AB system, as defined for photon proportional detection systems in Fukugita et al. (1996) (see their equation 7). We have converted from our *HST*-based photometric system to AB by determining the AB magnitude of Vega.

The mean absolute value of the residuals between the observed and synthetic photometry are within 0.025 mag for the *ugri* bands within SDSS DR12, completely in line with the 2–3% systematic error associated with the absolute calibration of the SDSS photometry onto the AB system.

The observed PanSTARRS photometry is from Tonry et al. (2012) and Schlafly et al. (2012), and adjusted by

the offsets reported in Scolnic et al. (2015). There are no measurements reported for SDSSJ102430.93. The residuals to the PanSTARRS photometry show a negative bias in the *y* band, however this bias is within $2 - -3\sigma$ of the large reported uncertainties of the photometry. The PanSTARRS 3pi survey images have significantly more cosmetic issues than the SDSS photometry, and careful analysis of these images with improved masking of diffraction spikes, ghosts, and cosmic rays will likely improve the agreement between the observed and synthetic photometry.

7. CONCLUSIONS AND DISCUSSION

We have presented the results from four faint DA white dwarfs that demonstrate the proposition that DA white dwarf fluxes as predicted from models are consistent with observations. This proposition has been the basis for *HST* calibrated fluxes for some time now. In this paper we have demonstrated that for fainter objects, where modest amounts of reddening must taken into account, the simple extension that includes solving for and applying individual self-determined reddening corrections over a wide range of wavelengths using a standard Milky Way reddening law works quite well, producing residuals of a few millimag. Nevertheless, there are several caveats to consider, some of which will be addressed in our continuing work as more data on more objects become available.

What our results really show is that the models accurately predict SED *ratios* between DA white dwarfs, i.e., the models are validated as *differential* predictors. It does not, however, test whether the models predict the absolute SEDs correctly. This is likely the dominant source of systematic uncertainty. We can get some purchase on it by comparing different sets of DA white dwarf models. A comprehensive discussion can be found in Bohlman et al. (2014), where current models are found to differ by more than 1% (and as much as 5%) short-ward of $0.27 \mu\text{m}$ and long-ward of $5 \mu\text{m}$. It is also possible that our understanding of the relevant atomic and atmospheric processes is yet incomplete. Nevertheless the validation of models as a good differential predictor of SEDs is already a tool that will enable us to calibrate photometric systems to a few millimag accuracy. The data we present here (and in future papers to come) will continue to anchor results, as model improvements and validation take place.

There are also additional caveats, but for these we have specific mitigation plans:

1. There are improvements underway to our processing steps. In particular, there is covariance between effective temperature and reddening. The data analysis flow is being redesigned to fit both these parameters (along with $\log g$) in the same process.
2. For the 9 targets observed in the *HST* GO-12967 (Cycle 20) program, there are additional photometric data being gathered in the Cycle 22 *HST* GO-13711 program. The additional images will not only secure the photometry, but an additional passband ($F275W$ in the near UV) will allow us to examine if the standard extinction law for reddening is indeed adequate.

TABLE 4
DERIVED AND FIDUCIAL APERTURE CORRECTIONS FOR *HST*
PASSBANDS

Passband	Aperture Correction Δ_T	Mean subtracted MAST Aperture Correction (mag)
F336W	0.011	0.033
F475W	−0.039	−0.023
F625W	−0.023	−0.024
F775W	−0.095	−0.020
F160W	0.060	0.064

TABLE 5
DA WHITE DWARF SYNTHETIC AND OBSERVED MAGNITUDES ON COMMON PHOTOMETRIC SYSTEMS

Survey	Target	Source ^a	u	g	r	i	z	y
					(mag) ^b			
DECam	SDSS-J010322.19	Syn	18.744	19.096	19.629	19.999	20.293	20.474
	SDSS-J102430.93	Syn	18.661	18.914	19.365	19.694	19.956	20.127
	SDSS-J120650.40	Syn	18.630	18.683	19.115	19.444	19.721	19.879
	SDSS-J163800.36	Syn	18.499	18.831	19.332	19.683	19.961	20.137
PS1 ^c	SDSS-J010322.19	Syn		19.109	19.573	19.938	20.212	20.484
		Obs		19.104 (0.007)	19.432 (0.016)	19.944 (0.021)	20.132 (0.032)	20.120 (0.124)
		Res		−0.005	−0.141	+0.006	−0.080	−0.364
	SDSS-J102430.93 ^d	Syn		18.925	19.315	19.642	19.886	20.136
	SDSS-J120650.40	Syn		18.689	19.065	19.386	19.643	19.888
		Obs		18.688 (0.007)	19.030 (0.010)	19.375 (0.014)	19.645 (0.026)	19.742 (0.052)
		Res		−0.001	−0.035	−0.011	+0.002	−0.146
	SDSS-J163800.36	Syn		18.843	19.279	19.628	19.886	20.147
		Obs		18.879 (0.008)	19.281 (0.010)	19.610 (0.011)	19.880 (0.021)	19.963 (0.101)
		Res		+0.036	+0.002	−0.018	−0.006	−0.184
	SDSS-J010322.19	Syn	18.657	19.045	19.553	19.918	20.255	
		Obs	18.66 (0.02)	19.03 (0.01)	19.54 (0.01)	19.94 (0.02)	20.37 (0.12)	
		Res	0.00	−0.02	−0.01	+0.02	+0.11	
SDSS	SDSS-J102430.93	Syn	18.597	18.874	19.296	19.623	19.922	
		Obs	18.57 (0.02)	18.84 (0.01)	19.28 (0.01)	19.58 (0.02)	19.77 (0.08)	
		Res	−0.03	−0.03	−0.02	−0.04	−0.15	
	SDSS-J120650.40	Syn	18.586	18.648	19.046	19.367	19.681	
		Obs	18.55 (0.02)	18.63 (0.01)	19.03 (0.01)	19.34 (0.02)	19.70 (0.10)	
		Res	−0.04	−0.02	−0.02	−0.03	+0.02	
	SDSS-J163800.36	Syn	18.418	18.783	19.259	19.608	19.925	
		Obs	18.44 (0.01)	18.81 (0.01)	19.28 (0.01)	19.58 (0.02)	19.79 (0.08)	
		Res	+0.02	+0.03	+0.02	−0.03	−0.14	

^a Synthetic magnitudes are labeled “Syn”. Observed magnitudes are provided where available and are labeled “Obs”. Uncertainties are provided in parentheses. Residuals between Observed and synthetic magnitudes are labeled by “Res”.

^b All magnitudes are on the AB system. The transmission/response function for each survey facility is calculated assuming an airmass of 1.3.

^c The PS1 observed magnitudes are from the calibration of [Tonry et al. \(2012\)](#) and [Schlafly et al. \(2012\)](#). They have been adjusted by the offsets in [Scolnic et al. \(2015\)](#). These offsets are $(\Delta g, \Delta r, \Delta i, \Delta z, \Delta y) = (0.020, 0.033, 0.024, 0.028, 0.011)$ mag.

^d There are no entries for SDSS-J102430.93 in the catalogs of [Tonry et al. \(2012\)](#) and [Schlafly et al. \(2012\)](#).

3. We are obtaining contemporaneous observations of all three *HST* primary standards, GD153, GD71 and G191B2B in our Cycle 22 program. This will allow us to tie our measurements directly on to the CALSPEC photometric scale, without the additional step of tying to the “Vegamag” scale, that in turn is tied to CALSPEC.
4. There has been little or no long term monitoring of these objects for constancy. We are seeking to pursue this from the ground.
5. It is known that a small fraction of DA white dwarfs have gaseous and planetary debris around them and some display pollution from metals (e.g., Koester et al. 2014). These can produce anomalous SEDs. Metal pollution is detectable only in the far UV. A program to observe our target DA white dwarfs with COS on *HST* would be necessary to constrain this potential systematic.
6. Magnetic fields have sometimes been observed in DA stars in our temperature range. The effect of such fields can be two fold. First, undetected Zeeman splitting in the Balmer lines can bias temperature and gravity determinations. Second, a rotating magnetic white dwarf can exhibit observable flux variations (Holberg & Howell 2011). Flux monitoring and spectroscopy of the H α line can flag the presence of such effects.

As a result of the above cautionary points, and with specific plans under way for their mitigation, we urge

that the results for the four DA white dwarfs presented in Tables 2 and 5 be treated as provisional. Nevertheless, we will be very surprised if they change by more than a percent and we publish them so that they can be tested by observers.

Some of the data presented in this paper were obtained from the Mikulski Archive for Space Telescopes (MAST). STScI is operated by the Association of Universities for Research in Astronomy, Inc., under NASA contract NAS5-26555. Support for MAST for non-*HST* data is provided by the NASA Office of Space Science via grant NNX13AC07G and by other grants and contracts.

Based on observations obtained at the Gemini Observatory, which is operated by the Association of Universities for Research in Astronomy, Inc., under a cooperative agreement with the NSF on behalf of the Gemini partnership: the National Science Foundation (United States), the National Research Council (Canada), CONICYT (Chile), the Australian Research Council (Australia), Ministério da Ciência, Tecnologia e Inovação (Brazil) and Ministerio de Ciencia, Tecnología e Innovación Productiva (Argentina) (Programs GS-2013A-Q-8 and GS-2013B-Q-22).

The authors thank the anonymous referee for incisive questions and helpful suggestions.

The authors wish to thank Dr. Annalisa Calamida for useful discussion and her critical reading of the paper.

Facilities: *HST* (WFC3, ACS), Gemini:South (GMOS), MMT (Blue Channel), Magellan:Baade (IMACS).

REFERENCES

- Bergeron, P., Saffer, R. A., & Liebert, J. 1992, *ApJ*, 394, 228
 Bertin, E., & Arnouts, S. 1996, *A&AS*, 117, 393
 Betoule, M., et al. 2014, *A&A*, 568, A22
 Blackwell, D. E., Leggett, S. K., Petford, A. D., Mountain, C. M., & Selby, M. J. 1983, *MNRAS*, 205, 897
 Bohlin, R. C. 2007, in *Astronomical Society of the Pacific Conference Series*, Vol. 364, *The Future of Photometric, Spectrophotometric and Polarimetric Standardization*, ed. C. Sterken, 315
 Bohlin, R. C. 2014, *AJ*, 147, 127
 Bohlin, R. C., & Gilliland, R. L. 2004, *AJ*, 127, 3508
 Bohlin, R. C., Gordon, K. D., & Tremblay, P.-E. 2014, *PASP*, 126, 711
 Dressler, A., et al. 2011, *PASP*, 123, 288
 Fitzpatrick, E. L. 1999, *PASP*, 111, 63
 Fukugita, M., Ichikawa, T., Gunn, J. E., Doi, M., Shimasaku, K., & Schneider, D. P. 1996, *AJ*, 111, 1748
 Gorecki, A., Abate, A., Ansari, R., Barrau, A., Baumont, S., Moniez, M., & Ricol, J.-S. 2014, *A&A*, 561, A128
 Hayes, D. S., & Latham, D. W. 1975, *ApJ*, 197, 593
 Holberg, J. B., & Bergeron, P. 2006, *AJ*, 132, 1221
 Holberg, J. B., Bergeron, P., & Gianninas, A. 2008, *AJ*, 135, 1239
 Holberg, J. B., & Howell, S. B. 2011, *AJ*, 142, 62
 Hook, I. M., Jørgensen, I., Allington-Smith, J. R., Davies, R. L., Metcalfe, N., Murowinski, R. G., & Crampton, D. 2004, *PASP*, 116, 425
 Horne, K. 1986, *PASP*, 98, 609
 Hubeny, I., & Lanz, T. 1995, *ApJ*, 439, 875
 Johnson, H. L., & Morgan, W. W. 1953, *ApJ*, 117, 313
 Koester, D., Gänsicke, B. T., & Farihi, J. 2014, *A&A*, 566, A34
 Li, T., DePoy, D. L., Marshall, J. L., Nagasawa, D. Q., Carona, D. W., & Boada, S. 2014, in *Society of Photo-Optical Instrumentation Engineers (SPIE) Conference Series*, Vol. 9147, *Society of Photo-Optical Instrumentation Engineers (SPIE) Conference Series*, 6
 Liebert, J., Bergeron, P., & Holberg, J. B. 2005, *ApJS*, 156, 47
 Matheson, T., et al. 2008, *AJ*, 135, 1598
 Mountain, C. M., Selby, M. J., Leggett, S. K., Blackwell, D. E., & Petford, A. D. 1985, *A&A*, 151, 399
 O'Donnell, J. E. 1994, *ApJ*, 422, 158
 Oke, J. B., & Schild, R. E. 1970, *ApJ*, 161, 1015
 Padmanabhan, N., et al. 2008, *ApJ*, 674, 1217
 Peterson, D. M., et al. 2006, *Nature*, 440, 896
 Querel, R. R., & Kerber, F. 2014, in *Society of Photo-Optical Instrumentation Engineers (SPIE) Conference Series*, Vol. 9147, *Society of Photo-Optical Instrumentation Engineers (SPIE) Conference Series*, 92
 Rauch, T., Werner, K., Bohlin, R., & Kruk, J. W. 2013, *A&A*, 560, A106
 Schlafly, E. F., et al. 2012, *ApJ*, 756, 158
 Schmidt, G. D., Weymann, R. J., & Foltz, C. B. 1989, *PASP*, 101, 713
 Scolnic, D., et al. 2015, *ApJ*, 815, 117
 Selby, M. J., Mountain, C. M., Blackwell, D. E., Petford, A. D., & Leggett, S. K. 1983, *MNRAS*, 203, 795
 Stone, R. P. S. 1977, *ApJ*, 218, 767
 Sullivan, M., et al. 2011, *ApJ*, 737, 102
 Suzuki, N., et al. 2012, *ApJ*, 746, 85
 Tonry, J. L., et al. 2012, *ApJ*, 750, 99